

Empirical Beam Hardening Correction for X-Ray Grating Interferometry (EBHC-GI)

5 Short title: Grating-Based Beam Hardening Correction

Brandon J. Nelson^{1,2}, Shuai Leng, Ph.D.², Elisabeth R. Shanblatt, Ph.D.², Cynthia H. McCollough, Ph.D.², Thomas Koenig, Ph.D.^{1,3}

1. Graduate Program in Biomedical Engineering and Physiology, Mayo Clinic Graduate School of Biomedical Sciences, Rochester, MN 55905
- 10 2. Department of Radiology, Mayo Clinic, Rochester, MN 55905
3. Ziehm Imaging, Lina-Ammon-Str. 10, 90471 Nuremberg, Germany

Corresponding author: Brandon J. Nelson

Mayo Clinic

15 200 First Street SW

Rochester, MN 55905

E-mail: nelson.brandon@mayo.edu

20 **This is the pre-peer reviewed version of the following article: Nelson, B.J., Leng, S., Shanblatt, E.R., McCollough, C.H. and Koenig, T. (2021), Empirical beam hardening and ring artifact correction for x-ray grating interferometry (EBHC-GI). Med Phys., which has been published in final form at <https://doi.org/10.1002/mp.14672>. This article may be used for non-commercial purposes in accordance with Wiley Terms and Conditions for Use of Self-Archived Versions.**

25 Abstract

Purpose: Talbot-Lau grating interferometry enables the use of polychromatic x-ray sources, extending the range of potential applications amenable to phase contrast imaging. However, these sources introduce beam hardening effects not only from the samples but also the gratings. In particular, grating inhomogeneities due to manufacturing imperfections can cause artifacts
30 when used with polychromatic sources. Consequently, the different energy dependencies of absorption, phase, and visibility contrasts impose challenges that so far have limited the achievable image quality. The purpose of this work was to develop and validate a correction strategy for grating-based x-ray imaging that accounts for beam hardening generated from both the imaged object and the gratings.

Methods: The proposed two-variable polynomial expansion strategy was inspired by work performed to address beam hardening from a primary modulator. To account for the multi-contrast nature of grating interferometry, this approach was extended to each contrast to obtain three sets of correction coefficients, which were determined empirically from a calibration scan. The method's feasibility was demonstrated using a tabletop Talbot-Lau gating interferometer
40 micro-CT system using CT acquisitions of a water sample and a silicon sample, representing low and higher atomic number materials. Beam hardening artifacts such as cupping and ring artifacts were quantified using mean squared error (MSE) from the beam-hardening-free target image and standard deviation within a reconstructed image of the sample. Finally, the pre-trained model developed using the water sample was applied to a fixated murine lung sample to demonstrate
45 robustness for similar materials.

Results: The water sample's absorption CT image was most impacted by beam hardening artifacts, but following correction to decrease ring artifacts, an 80% reduction in MSE and 57%

reduction in standard deviation was observed. The silicon sample created severe artifacts in all contrasts, but following correction, MSE was reduced by 94% in absorption, 96% in phase, and 90% in visibility images. These improvements were due to the removal of ring artifacts for all contrasts and reduced cupping in absorption and phase images and reduced capping in visibility images. When the water calibration coefficients were applied to the lung sample, ring artifacts most prominent in the absorption contrast were eliminated.

Conclusions: The described method, which was developed to remove artifacts in absorption, phase, and normalized visibility micro-CT images due to beam hardening in the system gratings and imaged object, reduced the MSE by up to 96%. The method depends on calibrations that can be performed on any system and does not require detailed knowledge of the x-ray spectrum, detector energy response, grating attenuation properties and imperfections, or the geometry and composition of the imaged object.

Keywords: grating interferometry, phase contrast, Talbot-Lau, ring artifacts, image quality, beam hardening

1. Introduction

X-ray phase and normalized visibility are the two novel contrasts accessible via grating interferometry that have gained attention due to their claimed improved contrasts in soft tissues and porous materials, respectively, when compared to traditional absorption radiography.¹⁻³ The use of Talbot-Lau grating interferometry⁴ broadens potential preclinical and clinical applications of simultaneously measuring x-ray absorption, differential phase, and normalized visibility by using polychromatic sources with greater tube output.⁵ This increased flux is particularly

70 important for reducing scan times in grating-based methods that lose x-ray intensity due to
grating absorption. However, the use of polychromatic sources comes at the cost of biasing
quantitative measurements by introducing beam hardening artifacts.⁶ While beam hardening is an
established area of study in x-ray absorption imaging, differences in grating-based systems and
derived contrasts contribute additional challenges, motivating the development of specialized
75 grating-based corrections.

Beam hardening is a consequence of the energy dependence of x-ray interactions particularly
in higher atomic number materials. In medical x-rays, energy-dependent absorption is
proportional to $\frac{1}{E^3}$, where E is the photon energy.⁷ In samples of finite thickness, this causes
polychromatic spectra to harden as lower energy x-rays are preferentially attenuated. The
80 remaining higher energy photons interact less and yield underestimated and inhomogeneous
absorption measurements. Similar effects exist for differential phase and normalized visibility
contrast mechanisms in polychromatic grating-based experiments.⁸ The degree of bias in phase
measurements differs from that of absorption due to the different physical contrast mechanisms⁹
and the different energy dependencies, which have been reported to be between $\frac{1}{E}$ and $\frac{1}{E^2}$ for
85 phase.^{10,11} In addition, while normalized visibility is sensitive to unresolvable microstructures, it
is also influenced by beam hardening.¹² Previous studies have shown normalized visibility to be
correlated with absorption and phase contrasts when using polychromatic spectra,¹³ suggesting
that the energy dependence of normalized visibility is also be influenced by energy dependencies
of absorption and phase. Therefore, despite presenting artifacts having a similar appearance,
90 beam hardening correction schemes developed for standard absorption imaging systems cannot
be directly applied to grating-based techniques because each contrast has a unique energy
dependence and hence requires its own correction.¹¹ Additionally, gratings with translucent

lamellae, a possible result of manufacturing errors,¹⁴ have been shown to further harden the beam and must also be considered in a correction scheme.⁹

95 A range of grating-based beam hardening correction strategies have been developed that address many of these challenges. Early corrections used specialized calibration phantoms to appropriately scale each contrast projection to match expected values for the given phantom geometry and composition.¹¹ Analytical methods overcome the need for phantom calibration scans but require detailed system knowledge of the source spectra and detector response, while
100 making assumptions on spectral responses of the sample and gratings.¹⁰

 To date these corrections have largely corrected beam hardening artifacts caused by the object being imaged; however, there remain additional challenges from grating-induced beam hardening that have not yet been adequately resolved. This additional source of beam hardening can originate from any grating with partial transmission or non-ideal phase modulation in their
105 lamellae, and this biases all three contrasts.⁹ One solution could be to design gratings with taller lamellae to further reduce transmission, but this comes at the cost of reducing absorption and visibility contrast-to-noise ratios.¹⁴ Further, partial transmission may be unavoidable in higher energy applications due to limitations in manufacturing gratings of sufficiently high aspect ratios.¹⁴

110 Dealing with beam hardening artifacts from gratings is uniquely challenging because they are spatially heterogeneous due to non-uniform lamellae thickness across the grating area. In a grating interferometer, depicted schematically in Fig. 1(a), this variation in lamellae thickness translates into locally varying levels of absorption, phase and visibility in the air scan images shown in Fig. 1(b). Due to the nonlinear nature of beam hardening, these local variations are not

115 completely removed from projections corrected using conventional flat-field methods once an
object has been inserted into the beam. Thus, a correction is needed that accounts for beam
hardening induced by both the sample and the gratings that also can be applied to each contrast
mechanism: absorption, differential phase, and normalized visibility. Additionally, because
grating inhomogeneities cannot be easily modeled or known *a priori*, a successful correction
120 method will require an empirical component.

The purpose of this work was to develop and validate such a correction strategy for grating-
based x-ray imaging that accounts for beam hardening generated from both the imaged object
and the gratings in all three contrasts. Experimental results using the proposed method are
reported for data acquired using a water sample and a silicon sample that exhibited more severe
125 beam hardening artifacts. Generalizability is then shown by applying the calibration coefficients
obtained for a water sample to micro-CT data of a murine lung sample. Finally, we discuss the
implications of this work for obtaining multi-contrast information with polychromatic sources.

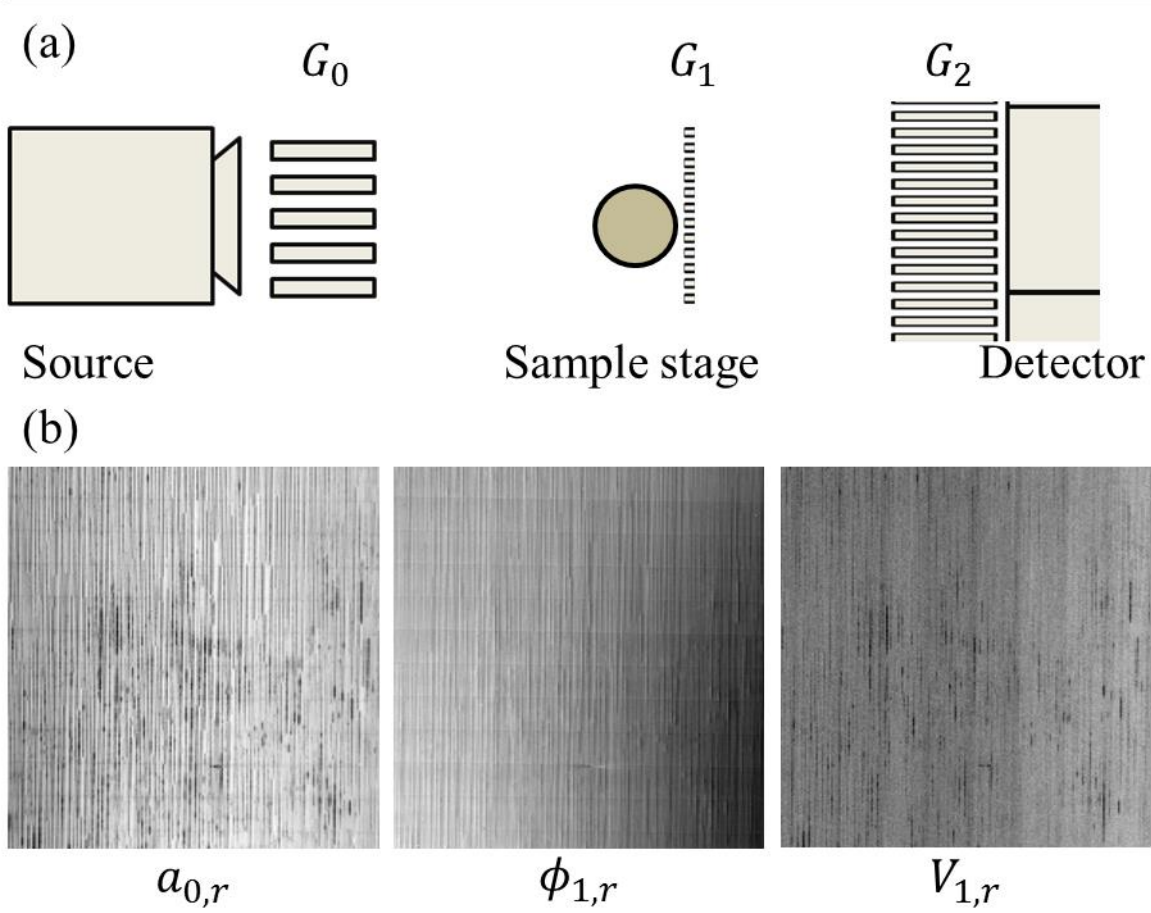


Fig. 1. Talbot-Lau grating interferometer (a). The source grating G_0 spatially modulates x-rays from a source with a large focal spot. G_1 produces a downstream Talbot carpet sensitive to phase shifts induced by samples present within the beam path. G_2 matches the period of the Talbot interference pattern at its location, allowing the sampling of the high frequency interference pattern with large detector apertures using phase stepping or Fourier retrieval techniques. Reference air scan images (b) $a_{0,r}$, $\phi_{1,r}$, $V_{1,r}$ for absorption, phase, and visibility, respectively, each showing visible grating structures.

2. Methods

2.1 Contrast-specific polynomial corrections

Polynomial corrections are one class of empirical beam hardening corrections for conventional (absorption) x-ray imaging that decomposes projections into a polynomial

representation. Such polynomial corrections are regression problems to find the function relating
 135 polychromatic projection measurements q to beam-hardening-free projection measurements p ,
 both determined from images of a calibration object with a known spectral response. Empirical
 Cupping Correction (ECC)¹⁵ is one such correction that assumes this function to be of the form

$$p = \sum_{i=0}^N c_i q^i, \quad (1)$$

for an N degree polynomial. Due to the linearity of the radon transform (denoted by R), the $N +$

140 1 correction coefficients c_i can be found in image space by minimizing for \mathbf{c}

$$\mathbf{c} = \operatorname{argmin}_{\mathbf{c}} \int d^3r w(\mathbf{r}) (\sum_{i=0}^N c_i f_i(\mathbf{r}) - t(\mathbf{r})). \quad (2)$$

Here $f_i(\mathbf{r}) = R^{-1}(q^i)$ are CT images reconstructed from projections q^i and $t(\mathbf{r})$ is the target
 image free of artifacts, representing the vector of voxels \mathbf{r} . The vector $w(\mathbf{r})$ is a binary mask
 used to exclude region boundaries sensitive to partial volume effects. This target image $t(\mathbf{r})$ is
 145 generated via the binary segmentation of any homogeneous region of material to be corrected
 from the original reconstructed image. By solving for the coefficient vector \mathbf{c} in image space the
 dependence on projection path length is removed, thus any phantom containing the material to be
 corrected for can be used without knowledge of its exact geometry for path length calculations.
 In addition, the computationally expensive step of reconstructing the images $f_i(\mathbf{r})$ is only
 150 required once for each monomial i , and hence the regression problem can be efficiently solved in
 image space.

Empirical Cupping Correction with a Primary Modulator (ECCP)¹⁶ is an extension of
 ECC developed to remove spatially dependent beam hardening artifacts generated by a primary

modulator. This is accomplished by adding a variable M representing projections of the system's

155 primary modulator such that Eq. (1) becomes

$$p = \sum_{ij} c_{ij} q^i M^j. \quad (3)$$

Similar to Eq. (2), coefficients c_{ij} are solved for in image space by minimizing

$$\mathbf{c} = \operatorname{argmin}_{\mathbf{c}} \int d^3r w(\mathbf{r}) (\sum_{ij} c_{ij} f_{ij}(\mathbf{r}) - t(\mathbf{r})), \quad (4)$$

with $f_{ij}(\mathbf{r}) = R^{-1}(q^i M^j)$ being the reconstructed images following elementwise multiplication

160 of projections q and primary modulator projections M raised to varying powers i and j .

Specifically, the modulator projections are a reference air scan generated as $M = -\ln(\frac{I_0}{I_r})$, where

I_0 denotes the x-ray intensity with only the modulator present, while I_r is the intensity measured without any modulator or sample.

In this work we demonstrate how this two-variable polynomial correction, ECCP, can be
 165 further adapted for use in grating interferometry, a technique we call Empirical Beam Hardening
 Correction for Grating Interferometry (EBHC-GI). EBHC-GI diverges from the previously
 described ECCP first by applying the two-variable polynomial correction introduced in ECCP to
 each contrast. Specifically, Eq. (3) and (4) become

$$p_k = \sum_{ij} c_{ijk} q_k^i M_k^j, \quad (5)$$

$$170 \quad \mathbf{c}_k = \operatorname{argmin}_{\mathbf{c}_k} \int d^3r w_k(\mathbf{r}) (\sum_{ij} c_{ijk} f_{ijk}(\mathbf{r}) - t_k(\mathbf{r})), \quad (6)$$

where subscript k represents the different contrasts, absorption, differential phase, and
 normalized visibility, and $f_{ijk}(\mathbf{r}) = R^{-1}(q_k^i M_k^j)$. Correction coefficients c_{ijk} are determined

separately for each contrast k in the image domain. Like ECCP, $t_k(\mathbf{r})$ is found by applying Otsu's method¹⁷ or a similar automatic binary segmentation technique to the original
175 reconstructed image for each contrast k . For the absorption and phase contrast channels, all values within each segmented region to be corrected are replaced with the median value within that region to approximate the desired beam-hardening-free value. By taking the median, large fluctuations from ring artifacts do not strongly influence the desired template value; however, severe cupping may still underestimate the true value to some degree. Similar to ECCP, a binary
180 mask $w_k(\mathbf{r})$ is used to remove partial volume effects at interfaces in the absorption and phase template images. In the case of the visibility contrast channel, the beam-hardening-free template assumes no contrast in homogenous regions, thus their constant value is set to 1.0, equal to air.

EBHC-GI deviates from ECCP again in its choice of spatial modulating term M . In the originally described ECCP method (Eq. 3), the term M is an absorption projection of the primary
185 modulator, acquired with no sample in the beam line, describing the spatial dependence of beam hardening induced by the primary modulator. However, in EBHC-GI the term M_k represents the influence of all three gratings for each image contrast. Extrapolating ECCP to each contrast mechanism suggests using each contrast k 's reference air scan, Fig. 1(b), for their respective M_k . Normalized visibility could be an exception as previous investigations have found polychromatic
190 measurements of normalized visibility to correlate with absorption and phase contrast in a system and material dependent manner.¹³ This suggests that grating-induced beam hardening artifacts in absorption and differential phase projections can contaminate normalized visibility projections. Thus the absorption or phase reference image could be a better descriptor of these grating-related beam hardening artifacts in the normalized visibility channel if this effect were
195 strong enough for a given system and material. This correlation of artifacts between contrasts

was experimentally investigated using our Talbot-Lau grating interferometer micro-CT system where we empirically determined M_V for the normalized visibility contrast (see Section 2.4).

2.2 Sample preparation

Three samples were evaluated in this study (Fig. 2): a water tube representing a low atomic number material (Fig. 2(a)), a silicon tile representing a higher atomic number material (Fig. 2(b)), as well as an excised and fixated murine lung (Fig. 2(c)) to demonstrate generalizability of the water coefficients. The water tube was a 1.5 mL Eppendorf snap tube filled with tap water. The silicon ($Z=14$) tile used was the lower portion of the spatial resolution module contained in a QRM micro-CT bar pattern phantom.¹⁸ The spatial resolution module in the phantom is etched into the top 100 μm of a 500 μm thick silicon tile shown schematically in Fig. 2(b). In this study we used the remaining 400 μm thick un-etched silicon region to evaluate the performance of the proposed method in a sample generating more severe beam hardening artifacts. Finally, the murine lungs used were excised from an *ex vivo* sample. All animal studies were approved by Mayo Clinic's Institutional Animal Care and Use Committee. The lungs were surgically removed, cannulated and instilled with a fixation solution of 50% PEG 400, 25% Ethyl alcohol, 10% formaldehyde and 15% water to a filling pressure of a 20 cm water column. The lungs were tied off at the trachea and immersed in the same solution for seven days before being air inflated at 25 mmHg and dried for 72 hours.¹⁹ The final product used for imaging is shown in Fig. 2(c). This fixation method preserves native air-tissue contrast as well as the inflated structure of the lung, and is a standard method for *ex vivo* structural imaging as determined by the American Thoracic Society guide on structural lung imaging.²⁰

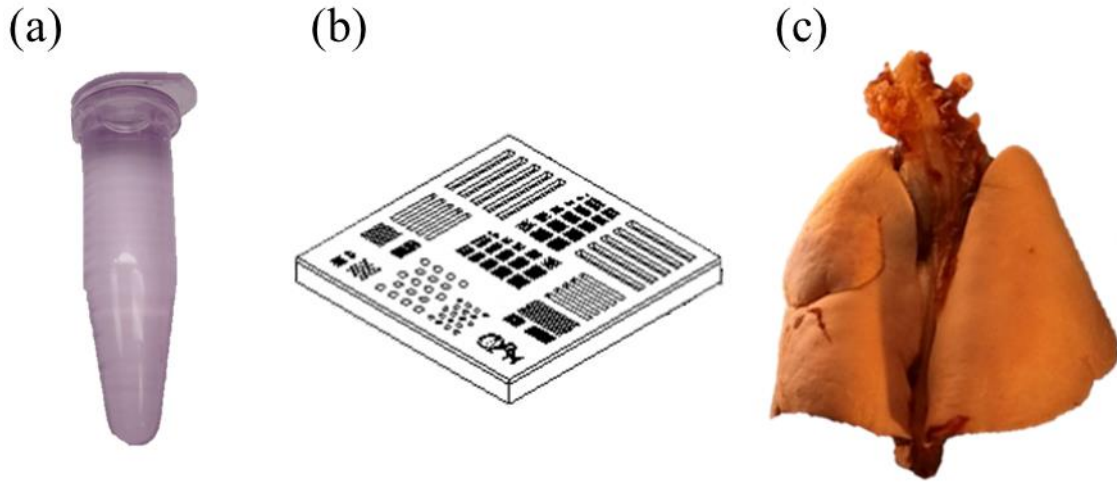


Fig. 2. Imaged samples include (a) 1.5 mL snap tube filled with water, (b) QRM micro-CT bar pattern phantom schematic adapted from Ref. 18. The lower 400 μm silicon region was the used in this study. (c) Posterior view of excised murine lung with heart following fixation and air drying at end-exhalation inflated volume.

2.3 Data acquisition and image reconstruction

The grating interferometer system used is shown schematically in Fig. 1(a) with gold Sunray design^{14,21} absorption gratings manufactured by Microworks GmbH (Karlsruhe, Germany). Further details about the source grating G_0 , the $\pi/2$ phase shift grating G_1 , and analyzer grating G_2 used in the study are listed in Table I.

Grating	Period (μm)	Duty cycle (%)	Lamellae material	Lamellae height (μm)	Size (cm^2)	Substrate material	Substrate thickness (μm)
G_0	10.0	55	Au	120	6 x 6	graphite	500
G_1	3.24	55	Au	2.6	6 x 6	Si	200
G_2	4.8	55	Au	120	6 x 6	graphite	500

Table I. Grating specifications of the experimental Talbot-Lau system. The lamellae heights are design heights and vary across a grating due to imperfections.

All measurements in this investigation used a Talbot-Lau geometry at the first Talbot distance with a G_0 to G_1 distance of 522 mm and a G_1 to G_2 distance of 251 mm. Mechanical phase stepping was performed to sample the Talbot interference pattern using a nano-OP65 piezoelectric stage (Mad City Labs, Madison, WI, USA) underneath G_1 . X-rays were generated from a Panalytical XRD source with a $400 \times 800 \mu\text{m}^2$ focal spot size on a tungsten anode operated at 55 kVp and 40 mAs filtered with a 200 μm thick beryllium window (spectra shown in Fig. 3). The detector used was a Princeton Instruments PIXIS 2048 CCD camera with native 13.5 μm pixels binned 4×4 and a 0.5 mm thick CsI(Th) single-crystal scintillator.

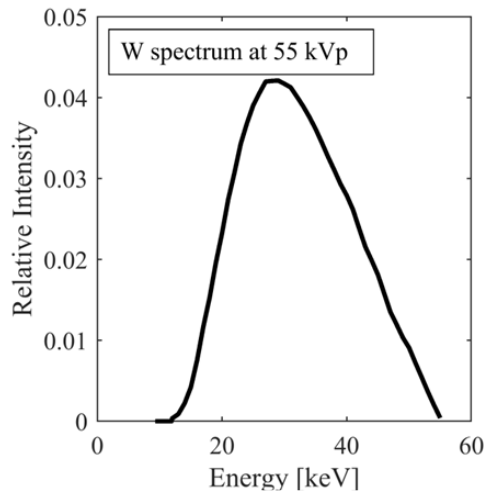


Fig. 3. Normalized source spectrum produced by a tungsten source operated at 55 kVp.

Sample and reference phase stepping curves (subscripted s and r , respectively) were generated by the phase stepping of G_1 in six steps of 1.5 seconds duration, each covering a single G_1 period. Projection data of various contrasts were then generated using one-dimensional Fast Fourier Transforms of the phase stepping curves acquired at each pixel.²² Absorption contrast A was calculated as the negative log ratio of the sample and reference zeroth order Fourier coefficients of the phase stepping curves, denoted a_0 ,

$$A = -\ln\left(\frac{a_{0,s}}{a_{0,r}}\right). \quad (7)$$

Differential phase $\Delta\phi$ was calculated as the phase difference between the first Fourier coefficients,

$$\Delta\phi = \phi_{1,s} - \phi_{1,r}. \quad (8)$$

Integral phase ϕ can then be determined by integrating the projection in the direction of phase stepping. Finally, visibility refers to the amplitude of the Talbot interference pattern relative to its baseline value, which for the reference phase stepping curve is calculated as $V_{1,r} = \frac{a_{1,r}}{a_{0,r}}$. We then define normalized visibility contrast V as the negative log ratio of the sample and reference phase stepping curve visibilities,

$$V = -\ln\left(\frac{V_{1,s}}{V_{1,r}}\right) = -\ln\left(\frac{a_{1,s}}{a_{0,s}} \frac{a_{0,r}}{a_{1,r}}\right). \quad (9)$$

In our experimental setup mean reference visibility was measured to be $V_{1,r} = 16.4\%$.

Using the aforementioned phase stepping and retrieval procedure, water, silicon, and murine lung samples were positioned with a source-to-isocenter distance of 710 mm and source-to-detector distance of 820 mm to perform CT. All CT acquisitions were performed over a full 360 degree range such that any ring artifacts would be presented as full rings. Due to the rotational symmetry of the water cylinder projection data were acquired every 2 degrees, while projections of both the silicon tile and fixed lung were acquired every 0.5 degrees. Images were then reconstructed using the FDK algorithm²³ as implemented in the TIGRE reconstruction suite.²⁴ In order to minimize image noise when determining correction coefficients, both the water cylinder and silicon tile images were reconstructed with TIGRE's Hamming filter while

lung images were reconstructed with a Ram-Lak filter appropriate for the high frequency features in the lungs.

2.4 Empirical determination of normalized visibility spatial modulating term M_V

265 Previous evidence has shown polychromatic normalized visibility measurements to be influenced by both absorption and phase properties in a material and system dependent manner¹³ thus we sought to determine M_V from Eq. (5) using the system and samples described in Sections 2.2, 2.3. To this end, repeat projections of the water and silicon samples were averaged to obtain low noise projections showing grating-induced beam hardening artifacts in each contrast. This
270 enabled low-noise comparisons of how artifacts in each contrast projection correlated to air scan grating projections like those shown in Fig. 1(b). To remove sample signal and focus on the high frequency grating-induced beam hardening artifacts projections were filtered with an edge-finding Laplacian filter with a 6 pixel wide square sliding window. For each contrast, pixel patches containing sample in the low-noise projections were selected and compared against the
275 corresponding air scan grating patches. Using these patches the Pearson correlation coefficient magnitude $|\rho|$ was calculated to evaluate how well each reference air scan patch correlated with the grating-induced beam hardening artifacts in each sample projection patch. The correlation magnitude $|\rho|$ is used because the solution to the interpolation problem finds the proper sign. For a given sample material we determined that the spatial modulating term for a given contrast k
280 should be the reference image r (where $r = a_{0,r}, V_{1,r},$ or $\phi_{1,r}$) that maximizes $|\rho|$ for a given contrast projection k , thus,

$$M_k = \operatorname{argmax}_r |\rho_{k,r}|. \quad (10)$$

Additionally, within each patch line profiles were taken perpendicular to the grating rule and compared to qualitatively confirm the results of Eq. (10). This procedure was performed to
 285 determine the spatial modulating term for normalized visibility M_V in both water and silicon samples as well as for the remaining contrasts to confirm our initial assumptions that $M_A = a_{0,r}$ and $M_{\Delta\phi} = \phi_{1,r}$.

A similar approach to finding the spatial modulating terms M_k would be to solve Eq. (6) determining coefficients c_{ijk} for each contrast k and reference image r for M_k and selecting the
 290 combination that yields the best correction as determined by the criteria described in Section 2.5. We argue, however, that the above approach of using low-noise projections and comparing correlations yields the same results while requiring fewer image reconstructions. We confirm this approach by determining the normalized visibility modulating term M_V using both described methods.

2.5 Evaluation of EBHCI-GI

After determining the grating term for normalized visibility M_V , sets of correction coefficients c_{ijk} were then calculated from the water sample and silicon sample image data as described by Eq. (6). In the water sample 2nd degree polynomial coefficients were determined for both variable dimensions resulting in 9 total coefficients for each contrast. For the higher atomic
 300 number silicon sample 3rd degree polynomial coefficients were determined for each variable yielding 16 coefficients per contrast. These coefficients were then applied to the original projection data and reconstructed into axial images for subsequent analysis.

The performance of our correction was quantified in terms of a reduction in the mean squared error (MSE) from the template image $t_k(\mathbf{r})$ and a reduction in standard deviation

measured in a central homogenous region of each sample image. These values were then used to compare the uncorrected and corrected images for each contrast. Line profile comparisons were also performed to visually compare the uncorrected, corrected, and template images.

Finally to assess the generalizability of the coefficients to similar materials we concluded our investigation by applying the coefficients determined from the water sample on the murine lung sample. Performance was assessed qualitatively for each contrast by visual inspection of uncorrected, corrected, and subtraction images.

3. Results

3.1 Determining the spatial modulating term M_V for normalized visibility

Quantitative correlation of grating-induced artifacts between sample and grating projections is shown as a correlation matrix in Fig. 4(a) for both water and silicon samples. The value of each entry in the matrix represents the correlation between each combination of sample and grating projection across image contrasts. Given that the sample water and silicon objects are mostly homogenous any residual signal following edge-enhancing filtering of the low noise projections can be assumed to be caused by grating-induced artifacts. These artifacts appear in the correlation matrix as elevated off-diagonal entries. Consistent with ECCP and our previous assumptions, the correlation of artifacts in absorption contrast is highest with its reference in both the water and silicon samples. Thus for both water and silicon samples from Eq. (7) we can determine the absorption grating term as $M_A = a_{0,r}$. For differential phase contrast enhanced off-diagonal elements were present for the silicon sample but not in water. In water we observed $|\rho_{\Delta\phi,V_{1,r}}| > |\rho_{\Delta\phi,\phi_{1,r}}|$, however given the low correlation and the limited influence of beam-hardening artifacts we can conclude that for differential phase contrast in water the choice

of grating term is less consequential. In the silicon sample these off-diagonal elements for differential phase $\Delta\phi$ are greatest with its reference $\phi_{1,r}$ and thus we can conclude $M_{\Delta\phi} = \phi_{1,r}$. However, for visibility contrast we observed $|\rho_{V,a_{0,r}}| > |\rho_{V,v_{1,r}}|$, suggesting that $M_V = a_{0,r}$. This
330 observation along with $|\rho_{V,\phi}| > |\rho_{V,v_{1,r}}|$ suggest a cross-contamination of absorption and phase information into the visibility contrast channel. These results are reflected qualitatively through line profile comparisons taken within the silicon sample in Fig. 4(b). The relatively lower correlation observed with V also suggests that using a single term M_V for visibility contrast may have a limited and potentially unsatisfactory effect.

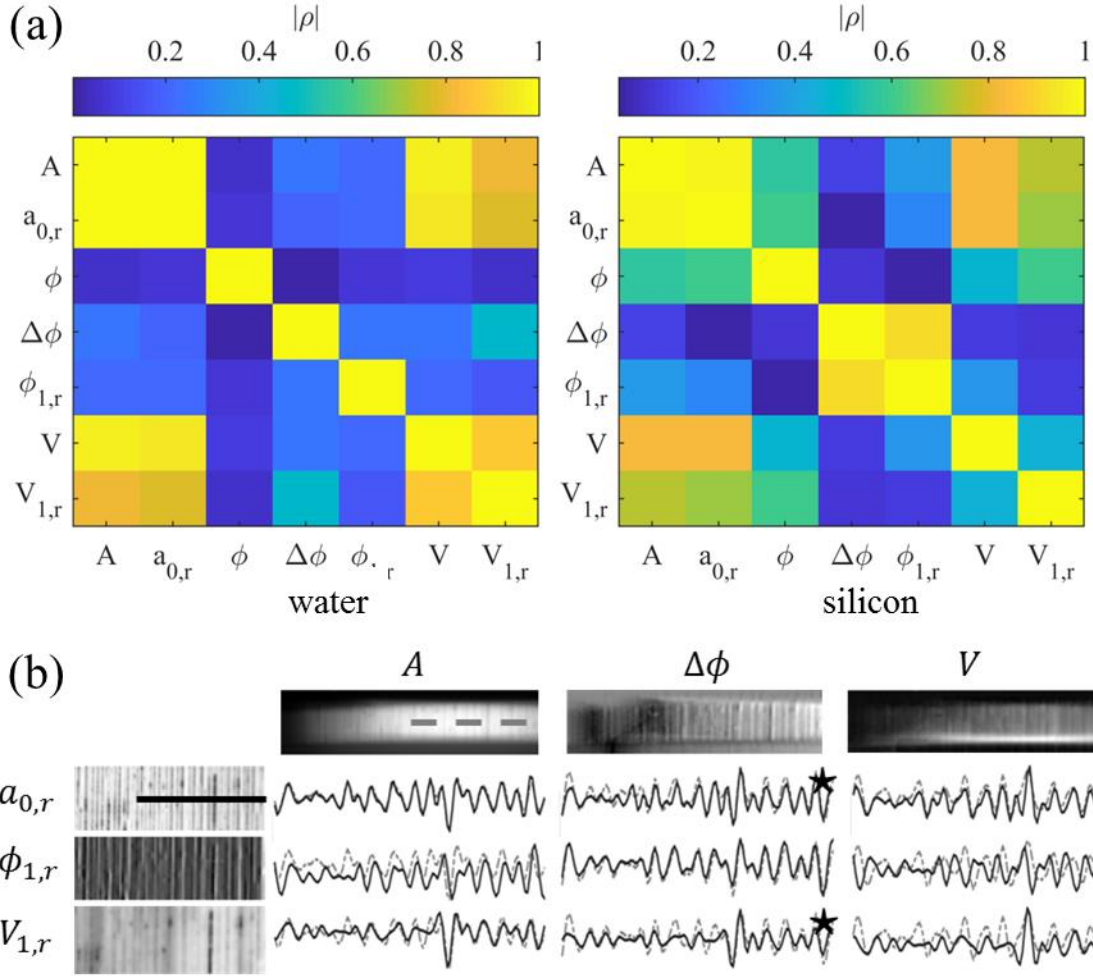


Fig. 4. (a) Correlation coefficient magnitudes $|\rho|$ between sample and air grating projections for both the water and silicon samples. Sample line profiles (b) from projections of the silicon tile show correlation between grating induced beam hardening artifacts in projections and reference images. Columns of a given sample contrast profile (dotted gray) are compared against each row of a given reference grating profile (black) for qualitative comparison. * indicates sign change and * indicates differentiation was performed to aid visual comparison.

3.2 Evaluation of EBHC-GI in water

Using the M_k grating terms determined for water in Section 3.1 fit coefficients for the water sample were determined using the original and template images shown in Fig. 5. Figure 6 then

compares the resulting images reconstructed from uncorrected projections and EBHC-GI

corrected projections. Line profile comparisons including the template image are included in Fig. 6(c). The measured MSE and standard deviation in the homogenous water region are presented in Table II. Most notably, while there is little evidence of cupping in any of the contrasts, there is a substantial amount of ring artifacts in the absorption contrast image that contributes to both the MSE and the noise reported in Table II. Of note, these ring artifacts are strongly suppressed following the application of EBHC-GI where the absorption MSE was decreased by 80% and standard deviation by 57%. In the normalized visibility channel, the influence of beam hardening is not obvious. Despite this, we measured a 65% reduction in the normalized visibility standard deviation following correction using $M_V = a_{0,r}$ compared to only a 58% reduction using $M_V = V_{1,r}$ with comparable reductions in MSE in both cases. In the phase contrast image, beam hardening effects are visually undetectable resulting in correspondingly small differences between the original and corrected images. These results suggest that for our given system in water, the absorption contrast is most strongly influenced by beam hardening and, in this low-Z imaging task, benefits most from EBHC-GI in terms of ring artifact reduction, reduced MSE from the template, and reduced standard deviation.

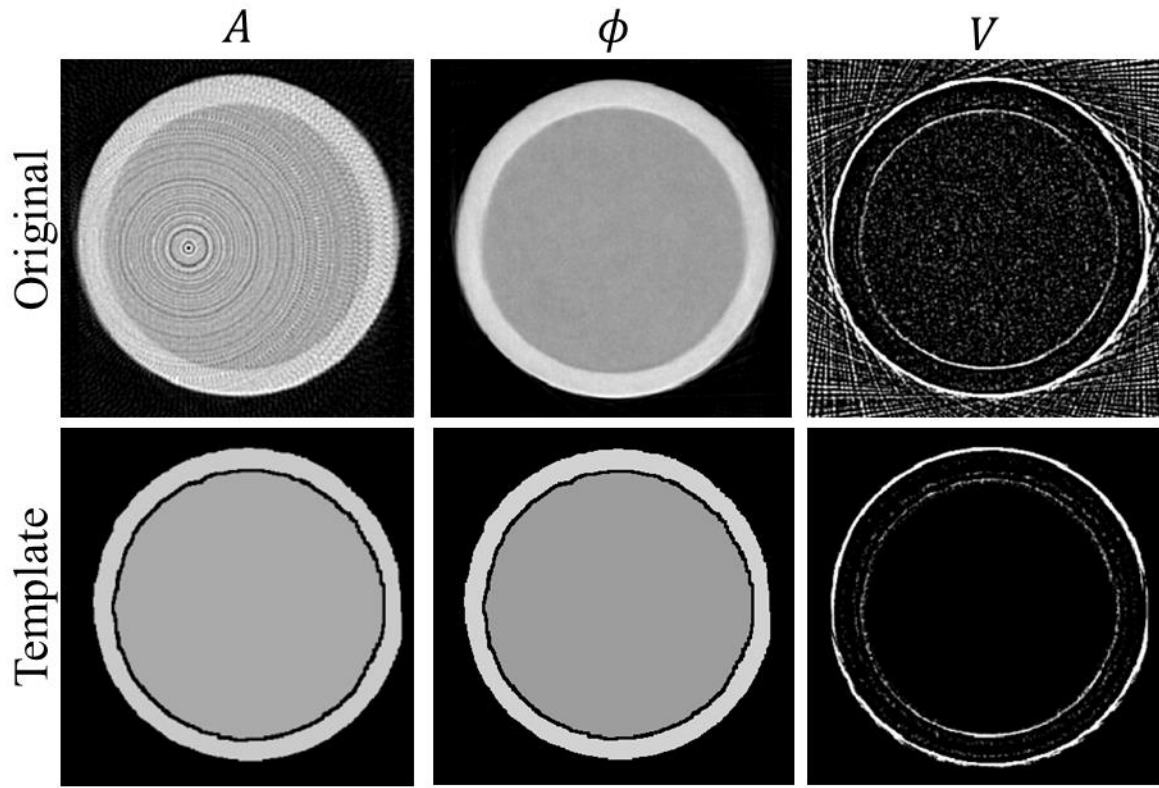


Fig. 5. Uncorrected reconstructions and artifact-free templates of the water sample for absorption A , phase ϕ , and normalized visibility V contrasts.

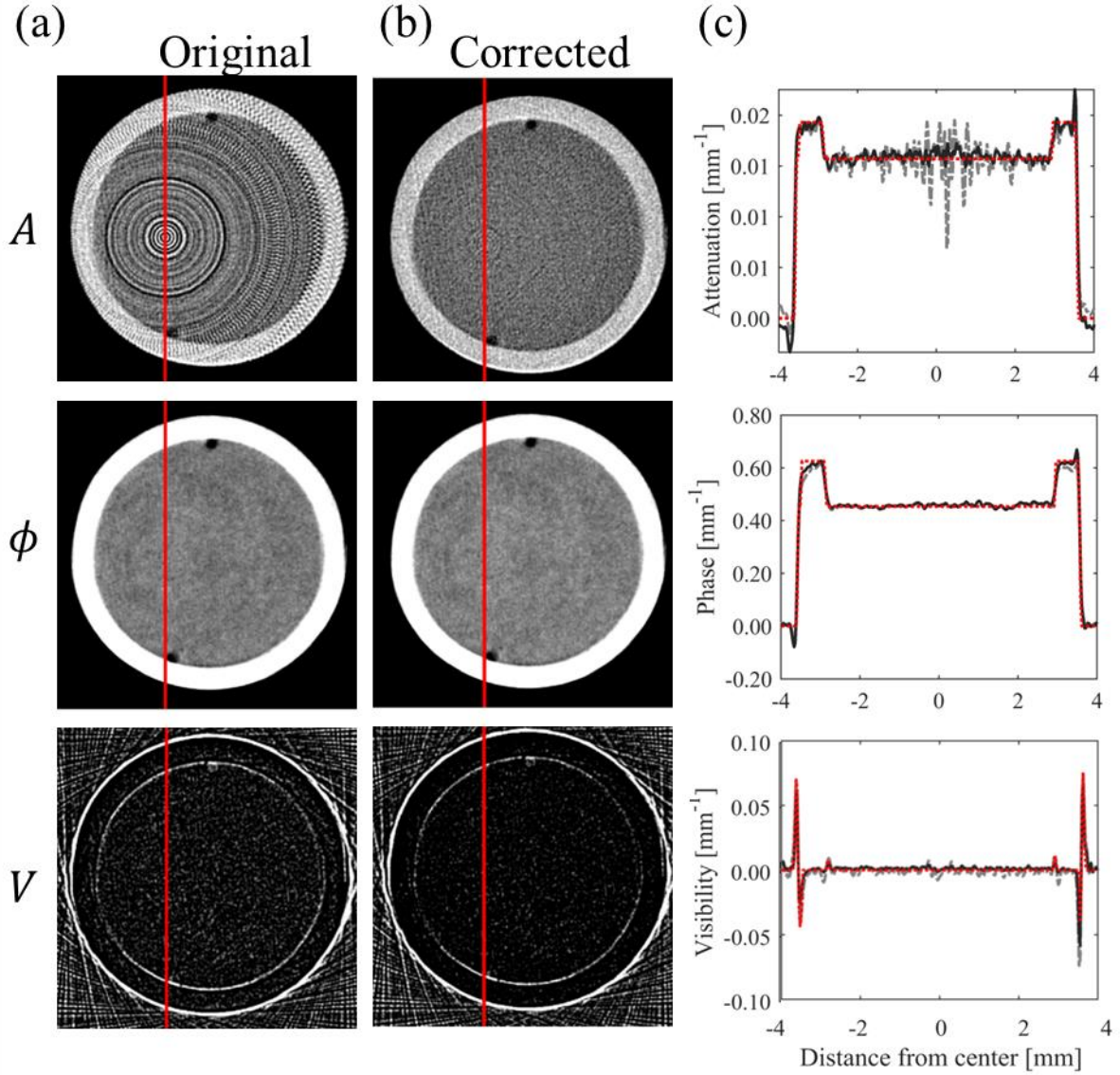


Fig. 6. Water sample reconstructions for each contrast with the original uncorrected axial image (a) shown left of the EBHC-GI corrected slice (b). The image display levels of each image are set to their means with a window width of four standard deviations. Column line profiles (c) compare original (dashed gray), corrected (solid black), and template (dotted red) line profiles.

Absorption			Phase			Visibility		
Image	MSE	Std dev	Image	MSE	Std dev	Image	MSE	Std dev
Original	1.33×10^{-6}	1.15×10^{-3}	Original	3.83×10^{-5}	6.02×10^{-3}	Original	7.58×10^{-6}	2.60×10^{-3}
Corrected	2.61×10^{-7}	4.85×10^{-4}	Corrected	3.63×10^{-5}	5.86×10^{-3}	Corrected	2.49×10^{-6}	8.86×10^{-4}
Change	-80.37%	-57.83%	Change	-5.22%	-2.66%	Change	-67.15%	-65.92%

360 Table II: Beam hardening correction results for water quantified in terms of mean squared error (MSE) from template t and standard deviation (Std dev) within the homogenous water region.

3.3 Evaluation in higher atomic number materials

Using correction coefficients c_{ijk} determined for silicon, image and line profile comparisons for each contrast from the original and corrected silicon sample projections are shown in Fig. 7 with MSE and standard deviation values reported in Table III. In the silicon tile images, all contrasts presented more severe artifacts than in water, with rings in each contrast, cupping in phase, and capping in the normalized visibility images. Furthermore, all three contrasts saw over 90% reductions in MSE. These results are an improvement over using the visibility reference $V_{1,r}$ for M_V which resulted in only an 88.2% reduction in MSE and 40% reduction in standard deviation from the uncorrected image. Both values are less than the 90% and 51% reductions reported in Table III for visibility using $M_V = a_{0,r}$, confirming the conclusions from the correlation analysis presented for silicon in Fig. 4.

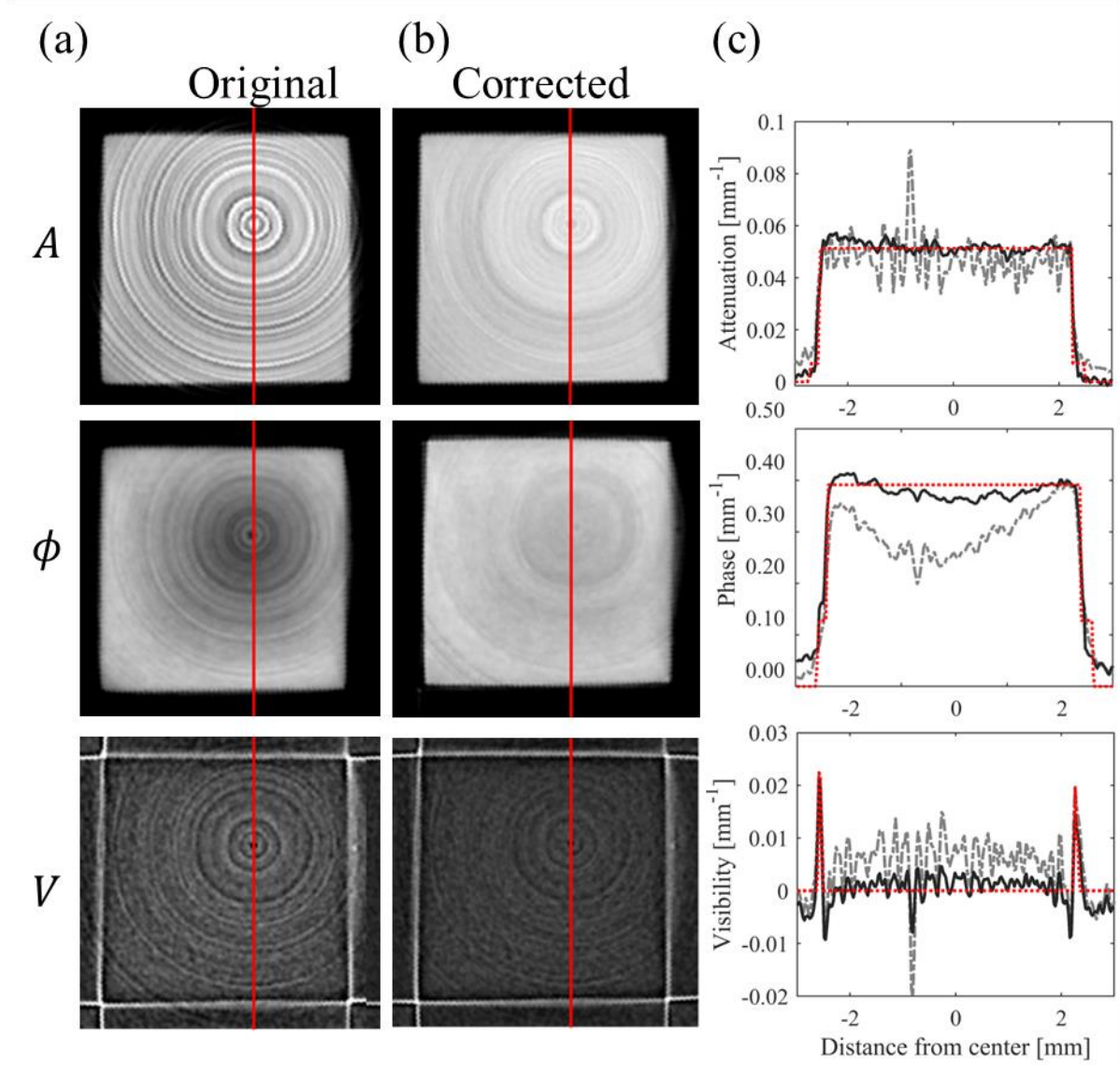


Fig. 7. Silicon tile reconstructions of attenuation, phase, and normalized visibility contrasts. Uncorrected images (a) are shown to the left of EBHC-GI corrected slices (b). The image display levels of each image are set to their means with a window width of four standard deviations. Column line profiles (c) compare original (dashed gray), corrected (solid black), and template (dotted red) line profiles.

Absorption			Phase			Visibility		
Image	MSE	Std dev	Image	MSE	Std dev	Image	MSE	Std dev
Original	6.76×10^{-5}	5.61×10^{-3}	Original	8.30×10^{-3}	3.62×10^{-2}	Original	5.15×10^{-5}	3.38×10^{-3}
Corrected	4.06×10^{-6}	1.94×10^{-3}	Corrected	2.67×10^{-4}	1.17×10^{-2}	Corrected	4.65×10^{-6}	1.65×10^{-3}
Change	-94%	-65.24%	Change	-96.78%	-67.68%	Change	-90.97%	-51.18%

375 Table III: Beam hardening correction results for silicon quantified in terms of MSE from the template and
standard deviation of values within the homogenous silicon region.

3.4 Lung imaging application

The original and corrected images of the murine lung specimen are shown approximately
midway through the mediastinum alongside difference images in Fig. 8. Similar to observations
380 in the water sample, the most noticeable artifacts were the rings in the original absorption image,
which were effectively eliminated in the corrected series. In the phase contrast series, there were
no visually observable changes between the original and corrected series, although the difference
image showed subtle signal changes. In the normalized visibility contrast images, there was
evidence of removed rings and non-edge signal changes in the difference image. Together, these
385 results in the murine lung sample are consistent with those seen in the water phantom, in
particular, that the absorption contrast was most susceptible to grating induced ring artifacts that
can be readily removed using EBHC-GI.

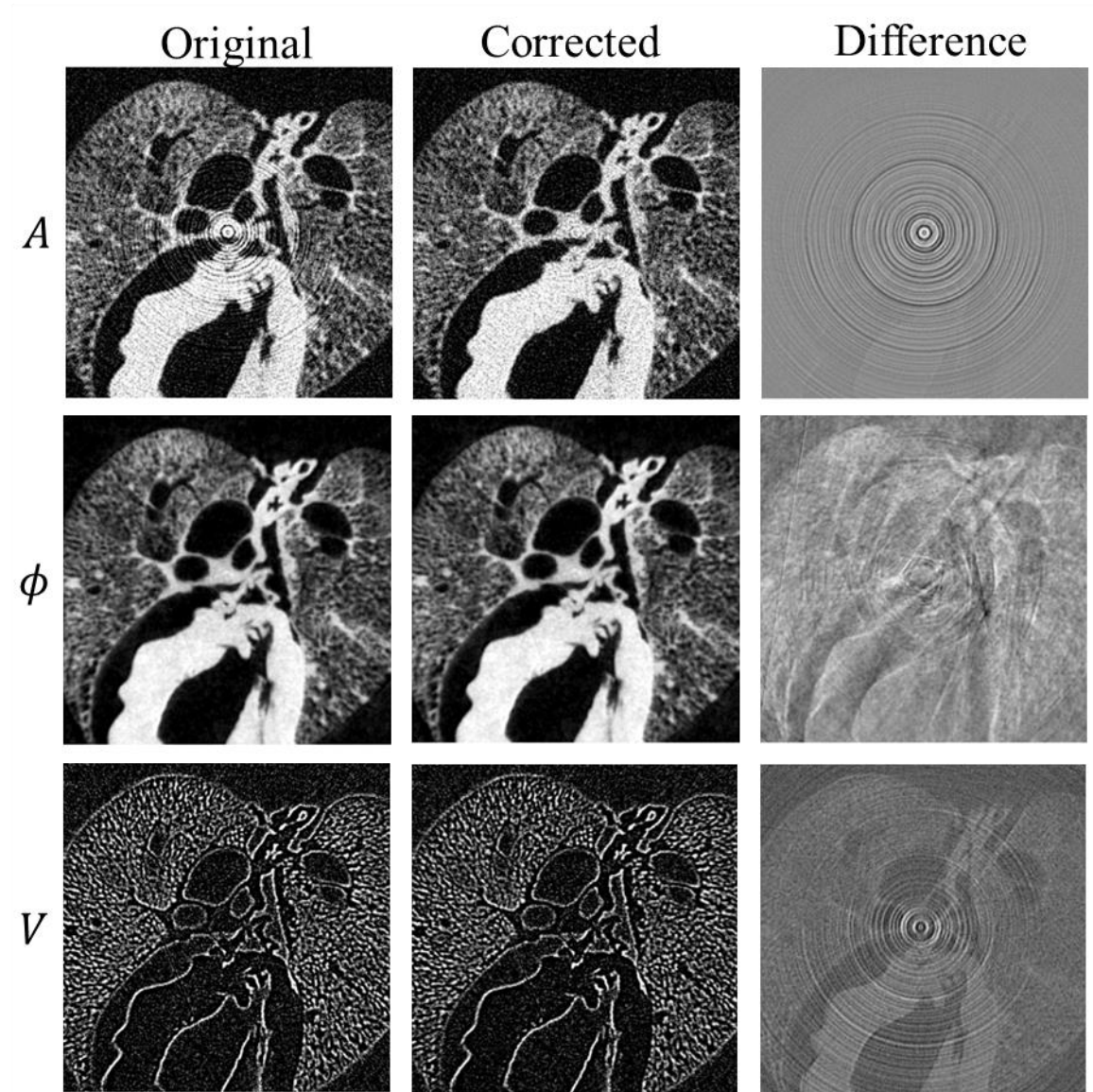


Fig. 8. Axial murine lung reconstructions in prone position show the heart, large airways, and lung parenchyma. Absorption, phase, and normalized visibility contrast images are shown both before and after correction along with a difference image.

390 4. Discussion

The key findings from our study are that beam hardening artifacts in grating-based x-ray phase contrast imaging can be largely suppressed by applying a two-variable polynomial correction to each of the derived contrasts. Specifically the two-variable approach includes both

sample projections and grating projections in each contrast so as to correct for both cupping or
395 capping artifacts derived from beam hardening in the sample as well as ring artifacts from beam
hardening in the gratings. The changes made to the originally-described ECCP¹⁶ included
applying the polynomial correction separately for each contrast mechanism to account for the
different energy dependencies of the different contrast mechanisms and using projections of the
system gratings instead of a primary modulator. We also showed methods to best determine this
400 grating-term for normalized visibility contrast which is influenced by both the imaging system
and sample.

In determining the grating term for normalized visibility contrast M_V using a correlation
analysis with grating projections we found for both materials studied that the normalized
visibility sample projections had the highest correlation with the absorption grating projections.
405 These results differ from directly extrapolating ECCP to each contrast, which would have
suggested using the reference visibility image $V_{1,r}$. However these observations of system and
material dependencies of grating-induced artifact in the normalized visibility contrast are
consistent with previous work that showed similar influence of absorption and phase information
in polychromatic measurements.¹³ In our particular investigations including the broad spectrum
410 used and materials studied we found beam hardening artifacts in the absorption contrast to have
greatest influence in normalized visibility projections. The cross-contamination between the
three contrast mechanisms that occurs due to beam hardening is but one of several sources of
bias in normalized visibility imaging present in grating based laboratory setups.^{12,25-27} In order to
perform better quantitative studies²⁸ of the small-angle-scattering and sub-resolvable structural
415 information contained in the visibility signal, these systematic influences must be understood and
accounted for. A limitation of our method in this regard is its empirical approach to generating

the template visibility image. Assigning known homogenous regions in our test objects to have a normalized visibility signal equivalent to air was necessary as it was unclear as to what would make an ideal visibility calibration object. This is coupled with the fact that the choice of an ideal
420 normalized visibility test object could likely be specific to material, energy and other systemic factors.²⁶

After determining the grating terms M_k and applying our found fit coefficients for each contrast and material our results demonstrated the benefit of applying a unique set of correction coefficients for each contrast. We saw this in varying contributions of cupping and ring artifacts
425 between materials and contrasts. The uncorrected water absorption image suffered most from grating-induced ring artifacts and needed a strong correction while the phase image required minimal correction. In the silicon tile we observed an even greater divergence of artifacts between the three contrasts. The silicon absorption image showed severe ring artifacts with modest cupping, while the phase image showed more severe cupping, and the visibility image
430 had modest capping and rings. This observation of unique energy dependence and presentation of beam hardening artifacts between contrasts and materials is consistent with previous work that showed similar dependencies.⁹

Like ECCP, our proposed method, EBHC-GI, is a first order correction and thus some rings remained due to detector gain inconsistencies or higher order beam hardening effects. Removing
435 these residual artifacts would be best handled with iterative methods¹⁰ adapted to account for spatially varying grating effects or additional image filtering.²⁹ Additionally for the normalized visibility contrast improved artifact reduction may be possible by first separating the influences of other contrasts.¹³ Another approach would be to add a second modulating term to include both

visibility and absorption. However, this comes at the cost of increasing the number of images
440 required to determine the correction coefficients.

Additionally, we demonstrated the generalizability of correction coefficients derived using one material with a similar atomic number. Our water corrections coefficients produced similar ring artifact removal in a murine lung sample as they did in a water sample.

Finally the push to enable human imaging with grating interferometry³⁰⁻³² requires higher x-
445 ray energies (e.g., high tube potential settings) and larger fields-of-view which places even higher demands on grating design and fabrication. Because partial transmission becomes unavoidable in these circumstances, and even desirable in others,^{14,33,34} our results demonstrate that image quality can be preserved for all three contrast mechanisms using a polychromatic x-ray source. This eases the requirements for grating design and fabrication and may facilitate
450 multi-contrast x-ray studies in humans.

5. Conclusions

In this investigation, we introduced an empirical correction for beam hardening in grating interferometry, EBHC-GI, that is an extension of a two-variable polynomial correction for primary modulators that we adapted to the unique contrast mechanisms and system properties of
455 a grating-interferometer. These adaptations included applying the polynomial correction to each contrast mechanism separately and determining optimal spatial modulating term for the normalized visibility contrast. In absorption and phase contrast images, this term was the reference projection data for each respective contrast mechanism. However, due to cross-contamination of absorption and phase contrast information into the visibility channel, the
460 optimal modulating term was determined for our system to be the absorption reference projection

data. Quantitative assessment of our method showed a reduction in beam hardening artifacts due to both the sample and the gratings in both water and silicon test objects, representing imaging of low- and higher-Z materials, respectively. This empirical method can be used, without the need of detailed system or sample knowledge, to correct for beam hardening effects in the sample and
465 in the gratings. Once determined, the coefficients can be used on all subsequent scans of like materials performed with similar acquisition settings.

6. Acknowledgements

The authors thank Jeffrey Meridew, Nunzia Caporarello Ph.D., and Daniel Tschumperlin Ph.D. for their help providing the murine sample used and Andrea Bracchetti for his help in
470 performing the fixation. We would also like to thank Marcus Zuber, Sabine Bremer, and the other members of the Laboratory for Applications of Synchrotron Radiation (LAS) at the Karlsruhe Institute for Technology for their help in testing the quality of our gratings. This work was funded by Mayo Clinic ASU Team Science Award and supported in part by the Mayo Clinic X-ray Imaging Research Core. We acknowledge the support of the CT Clinical Innovation
475 Center and the Mayo Clinic Graduate School of Biomedical Sciences.

7. Conflict of Interest

Research support is provided to the Mayo Clinic from Siemens Medical Solutions, USA, unrelated to this work. At the time of publication, Dr. Shanblatt is an employee of Siemens Healthcare. Thomas Koenig is an employee of Ziehm Imaging. The remaining authors have no
480 relevant conflict of interest to disclose.

8. References

1. Donath T, Pfeiffer F, Bunk O, et al. Toward clinical X-ray phase-contrast CT: demonstration of enhanced soft-tissue contrast in human specimen. *Invest Radiol*. 2010;45(7):445-452.
2. Bech M, Jensen TH, Feidenhans'l R, Bunk O, David C, Pfeiffer F. Soft-tissue phase-contrast tomography with an x-ray tube source. *Physics in Medicine and Biology*. 2009;54(9):2747-2753.
3. Momose A, Takeda T, Itai Y, Hirano K. Phase-contrast X-ray computed tomography for observing biological soft tissues. *Nat Med*. 1996;2(4):473-475.
4. Pfeiffer F, Weitkamp T, Bunk O, David C. Phase retrieval and differential phase-contrast imaging with low-brilliance X-ray sources. *Nat Phys*. 2006;2(4):258-261.
5. Bravin A, Coan P, Suortti P. X-ray phase-contrast imaging: from pre-clinical applications towards clinics. *Phys Med Biol*. 2013;58(1):R1-35.
6. Brooks RA, Di Chiro G. Beam hardening in x-ray reconstructive tomography. *Phys Med Biol*. 1976;21(3):390-398.
7. Attwood DT, Sakdinawat A, Geniesse L. *X-rays and extreme ultraviolet radiation : principles and applications*. Second edition. ed. Cambridge, United Kingdom ; New York, NY: Cambridge University Press; 2016.
8. Engelhardt M, Kottler C, Bunk O, et al. The fractional Talbot effect in differential x-ray phase-contrast imaging for extended and polychromatic x-ray sources. *J Microsc-Oxford*. 2008;232(1):145-157.
9. Munro PRT, Olivo A. X-ray phase-contrast imaging with polychromatic sources and the concept of effective energy. *Phys Rev A*. 2013;87(5).
10. Yan AM, Wu XZ, Liu H. Beam hardening correction in polychromatic x-ray grating interferometry. *Optics Express*. 2017;25(20):24690-24704.
11. Chabior M, Donath T, David C, et al. Beam hardening effects in grating-based x-ray phase-contrast imaging. *Med Phys*. 2011;38(3):1189-1195.
12. Yashiro W, Vagovic P, Momose A. Effect of beam hardening on a visibility-contrast image obtained by X-ray grating interferometry. *Opt Express*. 2015;23(18):23462-23471.
13. Pelzer G, Anton G, Horn F, et al. A beam hardening and dispersion correction for x-ray dark-field radiography. *Med Phys*. 2016;43(6):2774-2779.
14. Trimborn B, Meyer P, Kunka D, et al. Imaging properties of high aspect ratio absorption gratings for use in preclinical x-ray grating interferometry. *Phys Med Biol*. 2016;61(2):527-541.
15. Kachelriess M, Sourbelle K, Kalender WA. Empirical cupping correction: a first-order raw data pre-correction for cone-beam computed tomography. *Med Phys*. 2006;33(5):1269-1274.
16. Grimmer R, Fahrig R, Hinshaw W, Gao H, Kachelriess M. Empirical cupping correction for CT scanners with primary modulation (ECCP). *Med Phys*. 2012;39(2):825-831.
17. Otsu N. Threshold Selection Method from Gray-Level Histograms. *Ieee T Syst Man Cyb*. 1979;9(1):62-66.
18. Langner O, Karolczak M, Rattman G, Kalender WA. Bar and Point Test Patterns Generated by Dry-Etching for Measurement of High Spatial Resolution in Micro-CT. Paper presented at: World Congress on Medical Physics and Biomedical Engineering2009; Munich, Germany.
19. Groskin SA, Heitzman ER. *Heitzman's the lung, radiologic-pathologic correlations*. 3rd ed. St. Louis: Mosby; 1993.
20. Hsia CC, Hyde DM, Ochs M, Weibel ER, Structure AEJTFoQAoL. An official research policy statement of the American Thoracic Society/European Respiratory Society: standards for quantitative assessment of lung structure. *Am J Respir Crit Care Med*. 2010;181(4):394-418.
21. Jürgen Mohr TG, Danays Kunka, Johannes Kenntner, Juerg, Leuthold JM, Joachim Schulz, and Marco Walter. High aspect ratio gratings for X-ray phase contrast imaging. Paper presented at: International Workshop on X-ray and Neutron Phase Imaging with Gratings2012; Institute of Multidisciplinary Research for Advanced Materials.
22. Weitkamp T, Diaz A, David C, et al. X-ray phase imaging with a grating interferometer. *Opt Express*. 2005;13(16):6296-6304.

23. Feldkamp LA, Davis LC, Kress JW. Practical Cone-Beam Algorithm. *J Opt Soc Am A*. 1984;1(6):612-619.
- 535 24. Biguri A, Dosanjh M, Hancock S, Soleimani M. TIGRE: a MATLAB-GPU toolbox for CBCT image reconstruction. *Biomed Phys Eng Expr*. 2016;2(5).
25. Yashiro W, Noda D, Kajiwar K. Effect of insufficient temporal coherence on visibility contrast in X-ray grating interferometry. *Opt Express*. 2018;26(2):1012-1027.
26. Koenig T, Zuber M, Trimborn B, et al. On the origin and nature of the grating interferometric dark-field contrast obtained with low-brilliance x-ray sources. *Phys Med Biol*. 2016;61(9):3427-3442.
- 540 27. Yashiro W, Momose A. Effects of unresolvable edges in grating-based X-ray differential phase imaging. *Opt Express*. 2015;23(7):9233-9251.
28. Bech M, Bunk O, Donath T, Feidenhans'l R, David C, Pfeiffer F. Quantitative x-ray dark-field computed tomography. *Phys Med Biol*. 2010;55(18):5529-5539.
- 545 29. Munch B, Trtik P, Marone F, Stampanoni M. Stripe and ring artifact removal with combined wavelet--Fourier filtering. *Opt Express*. 2009;17(10):8567-8591.
30. Willer K, Fingerle AA, Gromann LB, et al. X-ray dark-field imaging of the human lung-A feasibility study on a deceased body. *PLoS One*. 2018;13(9):e0204565.
- 550 31. Horn F, Leghissa M, Kaeppler S, et al. Implementation of a Talbot-Lau interferometer in a clinical-like c-arm setup: A feasibility study. *Sci Rep*. 2018;8(1):2325.
32. Hauke C, Bartl P, Leghissa M, et al. A preclinical Talbot-Lau prototype for x-ray dark-field imaging of human-sized objects. *Med Phys*. 2018;45(6):2565-2571.
33. Wang ZT, Hauser N, Kubik-Huch RA, D'Isidoro F, Stampanoni M. Quantitative volumetric breast density estimation using phase contrast mammography. *Physics in Medicine and Biology*. 2015;60(10):4123-4135.
- 555 34. Meinel FG, Schwab F, Schleede S, et al. Diagnosing and mapping pulmonary emphysema on X-ray projection images: incremental value of grating-based X-ray dark-field imaging. *PLoS One*. 2013;8(3):e59526.